ChemCatChem

Research Article
doi.org/10.1002/cctc.202500438

Chemistry Europe
European Chemical Societies Publishing

www.chemcatchem.org

Growth of Carbon Nanotubes on Co(x)-Ni(1-x) Ferrites by Chemical Vapor Deposition and Performance on Catalytic Wet Peroxide Oxidation

Adriano S. Silva,*[a, b, c, d] Fernanda F. Roman,[a, c, d] Jose L. de Diaz de Tuesta,[e, f] Lola G. Olias,[e] Ihsan Çaha,[g] Ana P. Ferreira,[a] Renata P. de Souza,[h] Francis Leonard Deepak,[g] Ana I. Pereira,[b] Adrián M. T. Silva,[c, d] and Helder T. Gomes*[a]

Upcycling plastic solid wastes (PSWs) into high-value carbon nanotubes (CNTs) offers a promising approach to sustainable material development. This study explores the synthesis of CNTs via chemical vapor deposition (CVD) using mixed cobalt-nickel-iron oxide catalysts supported on alumina and PSW representative polyolefins as carbon sources. The impact of catalyst composition on the yield, morphology, and textural properties of CNTs was systematically evaluated. Characterization techniques, such as textural properties, transmission electron microscopy (TEM), Raman spectroscopy, and thermogravimetric analysis (TGA), revealed that increasing cobalt content in the catalyst resulted in thicker CNT walls (9.2–23.6 nm) and different textural properties (S_{BET} = 47–87 m^2 g^{-1}). The synthesized CNTs were then tested in catalytic wet peroxide oxidation (CWPO) for the degradation of sulfamethoxazole (SMX) and bisphenol A (BPA) in both single- and multi-component systems. The results indicated that a higher cobalt content in the CNT catalysts enhanced catalytic activity, particularly for BPA degradation, due to improved H_2O_2 decomposition. However, a higher leaching of Co and Fe was also observed. The CNTs synthesized with a Co/Ni catalyst composition ratio of 7/3 (CNT@$Co_{0.7}Ni_{0.3}$) exhibited the best balance among the tested materials in terms of CNTs yield, catalytic activity, and stability. These findings provide valuable insights to optimize CNT catalysts derived from waste plastics for environmental remediation applications.

1. Introduction

Plastic upcycling via the synthesis of nanostructured materials, such as carbon nanotubes (CNTs), has been explored in the literature[1] Some works have already investigated different aspects of the synthesis procedure, such as the acid washing effect on CNTs[1] and the use of different polymeric sources such as low-density polyethylene (LDPE), high-density polyethylene (HDPE), and polypropylene (PP), the most representative polymers in PSW.[2–5] The successful synthesis of CNTs using a single polymeric composition has already been demonstrated,[6] considering a one-chamber reactor and iron oxide supported on alumina as a catalyst; the obtained CNTs showed uncontrolled sizes and shapes, yielding approximately 20 wt.%.[6] Since the catalyst plays a crucial role in the growth of CNTs via chemical vapor deposition (CVD), optimizing its composition, dispersion, and substrate interactions is essential.[7–9] Transition metals (Ni, Fe, Co, Mo, Cu) are commonly used, with bimetallic catalysts often enhancing yield.[10–12] Additionally, the choice of substrate, commonly Al_2O_3, affects CNT growth mechanisms, which can follow tip growth (weak metal-support interaction) or base growth (strong interaction).[13–19]

[a] A. S. Silva, F. F. Roman, A. P. Ferreira, Prof. H. T. Gomes
CIMO, LA SusTEC, Instituto Politécnico de Bragança, Campus de Santa Apolónia, Bragança 5300-253, Portugal
E-mail: adriano.santossilva@ipb.pt
htgomes@ipb.pt

[b] A. S. Silva, Prof. A. I. Pereira
CeDRI, SusTEC, Instituto Politécnico de Bragança, Campus de Santa Apolónia, Bragança 5300-253, Portugal

[c] A. S. Silva, F. F. Roman, Prof. A. M. T. Silva
LSRE-LCM, Laboratory of Separation and Reaction Engineering – Laboratory of Catalysis and Materials, Faculty of Engineering, University of Porto, Rua Dr. Roberto Frias, Porto 4200–465, Portugal

[d] A. S. Silva, F. F. Roman, Prof. A. M. T. Silva
Associate Laboratory in Chemical Engineering, Faculty of Engineering (ALiCE), Faculty of Engineering, University of Porto, Rua Dr. Roberto Frias, Porto 4200–465, Portugal

[e] Prof. J. L. de Diaz de Tuesta, Dr. L. G. Olias
Chemical and Environmental Engineering Group. ESCET, Universidad Rey Juan Carlos, c/Tulipán s/n, Móstoles 28933, Spain

[f] Prof. J. L. de Diaz de Tuesta
Instituto de Investigación de Tecnologías para la Sostenibilidad, Universidad Rey Juan Carlos, C/Tulipán s/n, Móstoles 28933, Spain

[g] Dr. I. Çaha, Dr. F. L. Deepak
Nanostructured Materials Group, International Iberian Nanotechnology Laboratory (INL), Avenida Mestre Jose Veiga, Braga 4715-330, Portugal

[h] Prof. R. P. de Souza
Federal University of Technology – Paraná, Campus Dois Vizinhos, Boa Esperança Road, km 04, Dois Vizinhos 85660-000, Brazil

Supporting information for this article is available on the WWW under https://doi.org/10.1002/cctc.202500438

The CNTs synthesized via this route have demonstrated potential applicability in wastewater treatment, especially catalytic wet peroxide oxidation (CWPO, or heterogeneous Fenton), a well-known advanced oxidation process (AOP).[6] Batch experiments with paracetamol (PCM) and continuous-mode experiments with sulfamethoxazole (SMX) demonstrated promising results. For instance, Diaz de Tuesta et al. reported CNTs achieving complete PCM removal within 8 h of reaction.[6] In another study, Santos Silva et al. showed that polymeric composite membranes loaded with CNTs removed more than 85% of SMX during 8 h of CWPO-enhanced filtration, reinforcing the efficiency of CNTs for degradation of micropollutants by CWPO.[20]

CWPO is based on the interaction between a suitable catalyst and H_2O_2 to generate hydroxyl radicals ($HO^{\bullet}$, $E° = 2.5–3.1\ V_{NHE}$[21]), which is recognized as a highly oxidizing and non-selective reactive species. The most commonly reported CWPO catalysts comprise a support, such as pillared clays,[22] carbon xerogels,[23] and zeolites[24] impregnated with metals. Recent reports also demonstrated the effective degradation of pollutants using carbon-based metal-free catalysts subjected to suitable surface modifications.[25] However, the synthesis of metal-free carbon materials can be complicated if one is genuinely aiming for completely metal-free materials involving expensive technologies (e.g., stereolithography 3D-printing[25]). Even reaching high carbon purity levels using traditional carbon materials requires additional steps for purification, in which acid solutions are employed most of the time.[20,24,26] Despite its effectiveness in removing the metal phase, acid-washing is not considered an environmentally friendly technique.

The so-called traditional metal-based catalysts in CWPO are often comprised of transition metals as active phases, such as Co,[27] Ni,[28] and Fe,[27] among others.[28,29] The main reason for the migration to catalysts with less metal in the structure is the loss of the active phase due to metal leaching and pollution of the treated water with metals.[30] However, several reports presented alternatives to metal-supported catalysts with metal-encapsulated structures, protecting the metal from leaching. For instance, Santos Silva et al. reported multi-core shell magnetic nanoparticles for the degradation of PCM by CWPO, achieving complete removal after 6 h of reaction with the best formulation.[31] In another work, Ribeiro et al. discussed the catalytic activity of bimetallic carbon-coated materials, achieving complete degradation of 4-nitrophenol in less than 2 h of reaction.[32] In general, bimetallic catalysts are recognized as more active toward pollutant degradation in CWPO reactions, for instance, due to the (i) improved access to active Fe species at the catalyst surface due to Co incorporation, (ii) metallic Co catalyzing H_2O_2 decomposition via $HO^{\bullet}$ radical formation, and (iii) enhanced Fe^{3+} reduction to Fe^{2+} facilitated by surface metallic Co.[32]

Therefore, this work explores the optimized synthesis of CNTs using, as catalysts, mixed Co and Ni phases supported on alumina. The metals were chosen due to the recognized activity of Co in CWPO reactions and the higher yield reported in the synthesis of CNTs by CVD using Ni-based catalysts. The recovered CNTs were washed with water and used to degrade SMX and bisphenol A (BPA) in single- and multi-component experiments.

Table 1. Co and Ni content in CVD catalysts.

CVD Catalyst	Ni Content (wt.%)	Co Content (wt.%)
Co_0Ni_1Fe/Al_2O_3	15.42	<LOD[a)]
$Co_{0.1}N_{0.9}iFe/Al_2O_3$	13.52	2.12
$Co_{0.3}Ni_{0.7}Fe/Al_2O_3$	10.73	4.61
$Co_{0.5}Ni_{0.5}Fe/Al_2O_3$	8.13	8.18
$Co_{0.7}Ni_{0.3}Fe/Al_2O_3$	5.32	11.55
$Co_{0.9}Ni_{0.1}Fe/Al_2O_3$	2.67	13.63
Co_1Ni_0Fe/Al_2O_3	<LOD[a)]	15.61

a) Below the limit of detection.

The effect of CVD catalyst composition and characterization results was discussed in detail, as well as the catalytic activity toward the degradation of the selected pollutants in single- and multi-component systems. The best catalyst was later defined regarding synthesis yields, catalytic activity, and metal leaching. Pseudo-first-order and pseudo-second-order kinetic modelling was also performed for all pollutants and H_2O_2 in single- and multi-component systems.

2. Results and Discussion

2.1. Characterization of the CVD Catalysts

The results obtained for the X-ray diffraction (XRD) analysis of selected samples (Co_1Ni_0Fe/Al_2O_3, $Co_{0.5}Ni_{0.5}Fe/Al_2O_3$, and Co_0Ni_1/Al_2O_3) are shown in Figure S1. The analysis revealed that all samples contain alumina, as expected, according to the COD card number 96–100–0060. Sample Co_1Ni_0Fe/Al_2O_3 showed a composition of 87% Al_2O_3 and 13% $CoFe_2O_4$ (reference card 96–591–0064 from COD). In contrast, sample Co_0Ni_1Fe/Al_2O_3 revealed a composition of 83% Al_2O_3 and 17% $NiFe_2O_4$ (reference card 96–591–0065 from COD). The results of the sample $Co_{0.5}Ni_{0.5}Fe/Al_2O_3$ in semi-quantitative analysis showed 84% Al_2O_3, 8% $CoFe_2O_4$ and 8% $NiFe_2O_4$. The identification of both ferrite phases in the material is important to confirm that the procedure can successfully yield ferrites supported on alumina. The differences between samples are hardly observed in the diffractograms due to the high amount of Al_2O_3 in all samples and the similarity between $CoFe_2O_4$ and $NiFe_2O_4$ signals, as can be seen in reference cards (Figure S1c,d, respectively). The semi-quantitative analysis also confirmed the same percentage of Ni and Co as desired according to the synthesis procedure, keeping the percentage of Al_2O_3 close to 85% in all catalysts analyzed. The results obtained for Co and Ni composition (determined by digestion and atomic absorption) in CVD catalysts are shown in Table 1.

Ni and Co content were determined considering the formation of $CoFe_2O_4$ and $NiFe_2O_4$ phases in all materials observed in the XRD. The results obtained for Co and Ni contents determination via digestion and atomic absorption revealed that the synthesis procedure can successfully achieve cobalt and nickel ferrite phases supported on alumina with different percentages.

Table 2. Textural properties of the CNTs and final yield in CNTs synthesis.

Material	S_{BET} (m^2 g^{-1})	V_T (cm^3 g^{-1})	Yield (wt.%)
CNT@Co_0Ni_1	87	0.28	40.19
CNT@$Co_{0.1}Ni_{0.9}$	67	0.21	34.34
CNT@$Co_{0.3}Ni_{0.7}$	54	0.13	30.84
CNT@$Co_{0.5}Ni_{0.5}$	54	0.18	28.37
CNT@$Co_{0.7}Ni_{0.3}$	51	0.12	23.60
CNT@$Co_{0.9}Ni_{0.1}$	50	0.13	21.49
CNT@Co_1Ni_0	47	0.13	19.63

In all materials, the metal phase yielded a ca. 15% metal phase, which was the aim of the stoichiometric plan for the synthesis procedure.

2.2. Characterization of the CNTs

The N_2 adsorption-desorption isotherms recorded for the CNTs are shown in Figure S2. All materials presented similar isotherms, with S_{BET} and V_{total} shown in Table 2. The surface area values varied from 47 to 87 m^2 g^{-1}, with total pore volumes in the range 0.13–0.28 cm^3 g^{-1}. The values found for these materials are lower than those previously reported (ca. 70–100 m^2 g^{-1}[6]), which is related to the alumina used in the synthesis procedure of the CVD catalyst, that is, with a lower surface area than the D10-10 catalyst used in other works.[6]

The results indicated a dependency between the amount of Ni used in the CVD catalyst formulation and the textural properties. Figure S3 shows that S_{BET} and V_{total} generally increase with the Ni content. The Ni amount in the CVD catalyst formulation also resulted in higher yields of CNTs (Table 2), in agreement with other reports.[11,33,34] Ni catalysts yield more CNTs in CVD due to their ability to decompose hydrocarbons, sustaining continuous nanotube growth.[35] The linear correlation for the Ni content and the CNTs yield ($r^2 = 0.97$) was higher than the correlation between Ni content and textural properties ($r^2 = 0.71$ with S_{BET} and $r^2 = 0.76$ with V_T).

TEM images were recorded for selected samples (CNT@Co_0Ni_1, CNT@$Co_{0.3}Ni_{0.7}$, CNT@$Co_{0.7}Ni_{0.3}$, and CNT@Co_1Ni_0) to understand if there was a significant difference in the conformation of the CNTs upon using different percentages of Ni and Co in the CVD catalyst (Figure 1). The results obtained revealed that CNT samples show a dependency between the number of walls and composition of the CVD catalyst, with ca. 15 walls for CNT@Co_0Ni_1, ca. 19 walls for CNT@$Co_{0.3}Ni_{0.7}$, ca. 21 walls for CNT@$Co_{0.7}Ni_{0.3}$, and ca. 26 walls for CNT@Co_1Ni_0. The walls of the CNTs can be seen with better resolution in Figures 1b (CNT@Co_0Ni_1), 1e (CNT@$Co_{0.3}Ni_{0.7}$), 1 h (CNT@$Co_{0.7}Ni_{0.3}$), and 1k (CNT@Co_1Ni_0Fe). A number of walls in the same range (14 to 37) was determined for CNT samples in a previous work,[6] but in that case there was no control over the synthesis procedure.

The CNTs had average diameters of 9.2 ± 3.5 nm for CNT@Co_0Ni_1 (Figure S4a), 12.8 ± 4.2 nm for CNT@$Co_{0.3}Ni_{0.7}$ (Figure S4b), 20.3 ± 1.5 nm for CNT@$Co_{0.7}Ni_{0.3}$ (Figure S4c), and

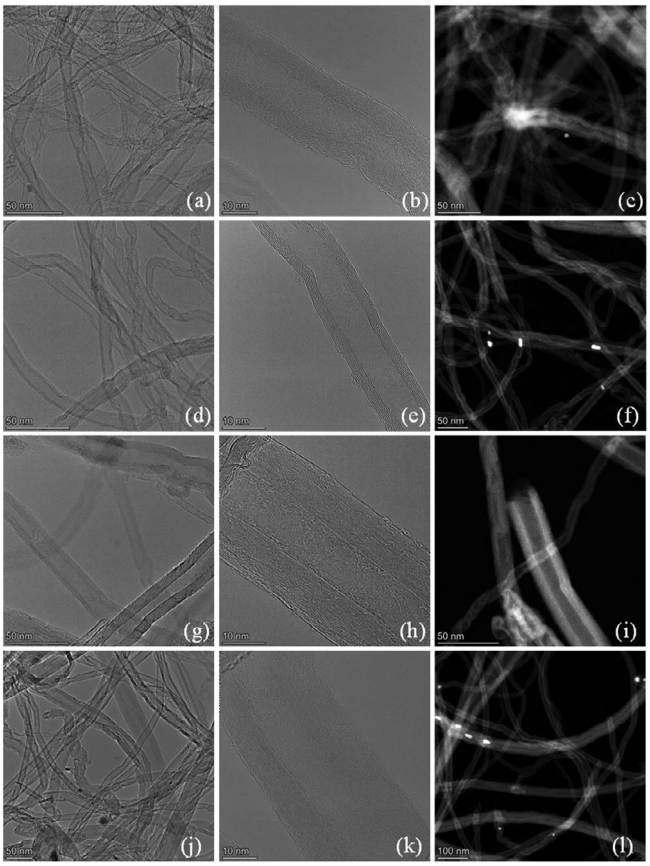

Figure 1. Results obtained for HR-TEM, higher magnification HR-TEM, and HAADF-STEM for samples: (a–c) CNT@Co_0Ni_1, (d–f) CNT@$Co_{0.3}Ni_{0.7}$, (g–i) CNT@$Co_{0.7}Ni_{0.3}$, and (j–l) CNT@Co_1Ni_0.

23.6 ± 6.2 nm for CNT@Co_1Ni_0 (Figure S4d). The diameter values obtained for these samples are smaller than those reported in previous works (28–33 nm).[6] The most likely cause of this difference is related to the CVD catalyst used in the synthesis procedure. In a previous study, IO/Al_2O_3 (IO = iron oxide) was a catalyst prepared following the sol-gel method in an oxidative atmosphere.[6] In these conditions, there is less control over the inorganic structures formed in the sol-gel process since the iron can undergo side reactions, resulting in a mixture of different iron phases over the Al_2O_3 support.[6] In contrast, the same methodology used to synthesize mixed cobalt and nickel oxides supported on Al_2O_3 will not be hindered by the oxidative atmosphere, ensuring a higher purity and nanoparticles with a narrow particle size distribution.

The increase in particle size and number of walls for higher contents of Co is related to the formation of cobalt and nickel oxides during the sol-gel process and the behavior of the nanoparticles during thermal treatment. Whereas $NiFe_2O_4$ is a soft magnetic material with lower coercivity,[36] $CoFe_2O_4$ is a hard magnetic material with higher anisotropy and a greater tendency for particle agglomeration,[37] reducing the effective surface area. In fact, $NiFe_2O_4$ nanoparticles tend to remain smaller and more thermally stable under CVD conditions, promoting the growth of narrower CNTs with fewer walls. Additionally, Ni^{2+} ions limit carbon solubility, resulting in more

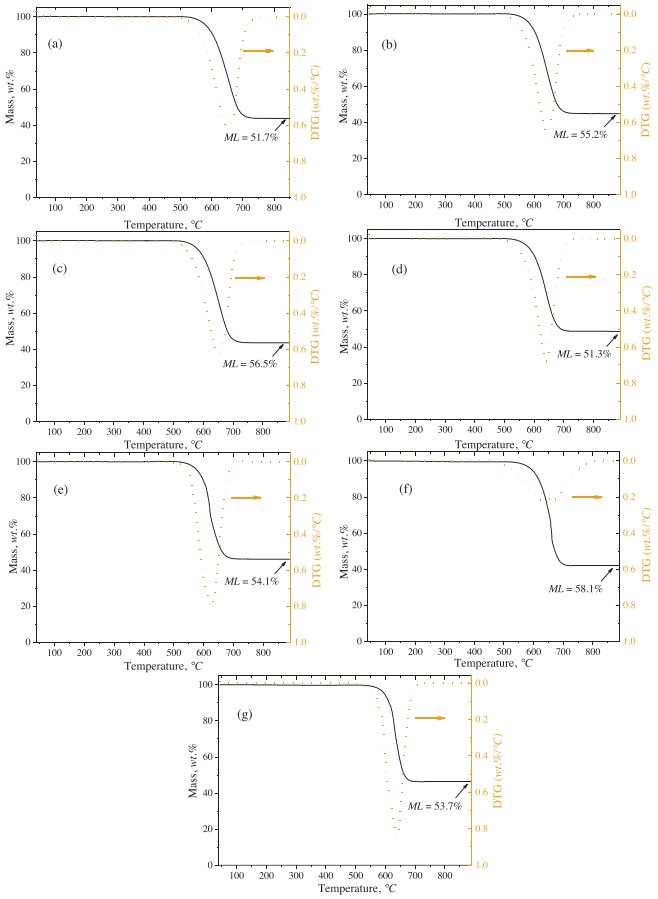

Figure 2. TGA and DTG results for samples: (a) CNT@Co_0Ni_1, (b) CNT@$Co_0.1Ni_{0.9}$, (c) CNT@$Co_{0.3}Ni_{0.7}$, (d) CNT@$Co_{0.5}Ni_{0.5}$, (e) CNT@$Co_{0.7}Ni_{0.3}$, (f) CNT@$Co_{0.9}Ni_{0.1}$, and (g) CNT@Co_1Ni_0.

controlled, layer-by-layer[36][] In contrast, $CoFe_2O_4$ particles are more prone to sintering, leading to larger catalytic sites and the formation of multi-walled CNTs with higher diameters.[38,39] Furthermore, it should also be noted that Ni^{2+} has a smaller ionic radius (0.63 Å) compared to Co^{2+} (0.74 Å), which can influence the nanoparticle size distribution on alumina and the mechanism of CNT growth during CVD.[40] Thus, increasing amounts of Co in the CVD catalyst will lead to average thicker CNTs. The correlation between the diameter of the CNTs obtained by CVD and Co and Ni contents in the CVD catalyst has not been reported before. However, it is known that such characteristics of the CVD catalyst can influence the growth of CNTs in other aspects as well (e.g., CNT curvature).[41,42] Figure S5 shows the correlation between Co amount and diameter, revealing that the average diameter of the CNTs will increase upon using more Co and less Ni in the CVD catalyst ($r^2 = 0.98$). The correlation was confirmed by comparing the average number of walls in CNT samples with the average diameter, as shown in Figure S6 ($r^2 = 0.89$).

The results obtained by TGA revealed no significant differences between the samples, as shown in Figure 2 (*ML = mass loss*).

The materials presented a similar TGA profile, with ash content varying from 51.3 to 56.5 wt.%. The high ash content from the material was expected due to the presence of the CVD metal catalyst from the synthesis procedure. No correlation between Ni and Co content in CVD catalysts and ash content was observed. Mass loss peaks at ca. 600 °C correspond to carbon material degradation, typically observed for CNTs.[1,6,43–46] The high oxidation resistance characteristic of ordered structured carbon materials was also observed for the samples of CNTs discussed in a previous study.[6] The deviation observed in DTG for sample CNT@$Co_{0.7}Ni_{0.3}$ is not concerning, considering the sensitivity of the analysis and the fact that despite widening, the peak center still coincides with other CNT samples. The results obtained from the elemental analysis are shown in Table 3 (nitrogen and sulfur contents were negligible).

The carbon content was above 53% in all materials evaluated, and no *N* or *S* were found, which was already expected. The C/H mass ratio was also similar for the different materials, with no influence from the CVD catalyst being observed. All materials had high C/H values, surpassing 2000 unities. This characteristic was not discussed in the previous report, but those CNT samples have C/H ratios in the range 480–920,[6] values considerably lower than when the CNTs are obtained with mixed cobalt ferrites CVD catalysts. According to the literature, higher C/H values can influence several properties of the CNTs, such as thermal and electrical conductivity, purity (fewer hydrogen-containing impurities or defects), and better-defined walls.[47–49] The results obtained for Ni and Co content revealed the presence of these metals in the CNTs, most likely encapsulated in CNT walls. The percentages are significantly lower than observed in the CVD catalyst, suggesting that washing the materials with

Table 3. Elemental analysis results for the CNTs and Co and Ni contents.

Material	C (wt.%)	H (wt.%)	C/H Mass Ratio	Co Content[a] (wt.%)	Ni Content[a] (wt.%)
CNT@Co_0Ni_1	57.1 ± 0.1	0.02 ± 0.00	3246	0	1.9
CNT@$Co_{0.1}Ni_{0.9}$	56.2 ± 0.6	0.02 ± 0.00	2466	0.2	1.88
CNT@$Co_{0.3}Ni_{0.7}$	57.2 ± 0.1	0.02 ± 0.00	2988	0.6	1.51
CNT@$Co_{0.5}Ni_{0.5}$	54.1 ± 0.9	0.01 ± 0.00	7821	0.9	0.98
CNT@$Co_{0.7}Ni_{0.3}$	54.3 ± 0.4	0.00 ± 0.00	9053	1.4	0.6
CNT@$Co_{0.9}Ni_{0.1}$	57.8 ± 1.1	0.03 ± 0.00	2080	1.9	0.2
CNT@Co_1Ni_0	53.8 ± 1.6	0.02 ± 0.00	2471	2.3	0

a) Determined based on CVD crystalline phase equivalents.

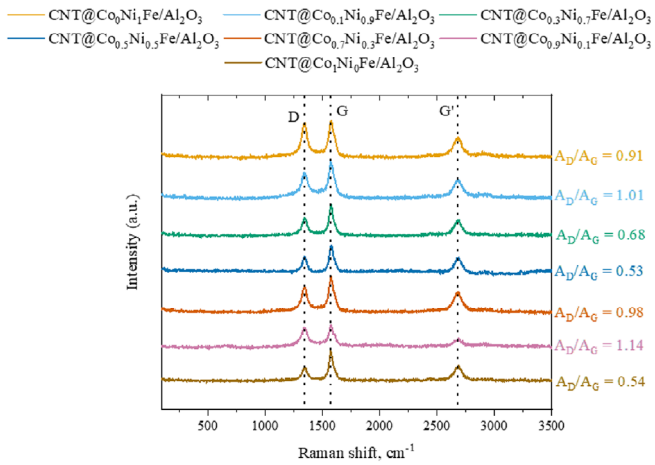

Figure 3. Raman spectra for all samples of CNTs.

water removed most of the Co and Ni contents that were not active during the growh of CNTs.

Figure 3 shows the results obtained for the Raman spectroscopy of the materials. The spectra have three evident peaks located at 1344 cm^{-1} (D band), 1603 cm^{-1} (G band), and 2677 cm^{-1} (G′ band). The D peak is ascribed to structure defects in the carbon material, and the G peak is related to the in-plane stretching of sp^2 carbon atoms, indicating a graphitic nature. The third peak found in all samples is characteristic of CNTs and is associated with the π band in the electronic structure.

The values calculated for A_D/A_G from the deconvolution indicate how ordered the material is. For instance, higher values represent materials with more structural defects than graphitic carbon, and the inverse is characteristic of materials with high graphitic carbon content. There is no correlation between the CVD catalyst used and the A_D/A_G observed, and the values agree with other works reporting Raman results for CNTs prepared from polymers.[1,50,51]

3. Performance in CWPO Batch Experiments

The experiments were carried out in three different systems: S1 was performed to evaluate the degradation efficiency of SMX, S2 assessed the degradation of BPA, and the third system (S3) comprised both pollutants with the same concentration used in single-component studies.

Kinetic modelling results for all systems will be briefly introduced before a more in-depth discussion of the experimental findings. The results for kinetic modelling using pseudo-first-order (PFO) and pseudo-second-order (PSO) models (Table S4) across all systems are presented in Tables S1 (SMX only, system S1), S2 (BPA only, system S2), and S3 (SMX and BPA, system S3). The PSO model provided a better fit across the three different systems, as indicated by the r^2 values in the tables and the parity plots in Figures S7–S9. However, differences in model performance were observed between single- and multi-component systems. The results showed that in system S1 (SMX only), the PSO model better described H_2O_2 decomposition,

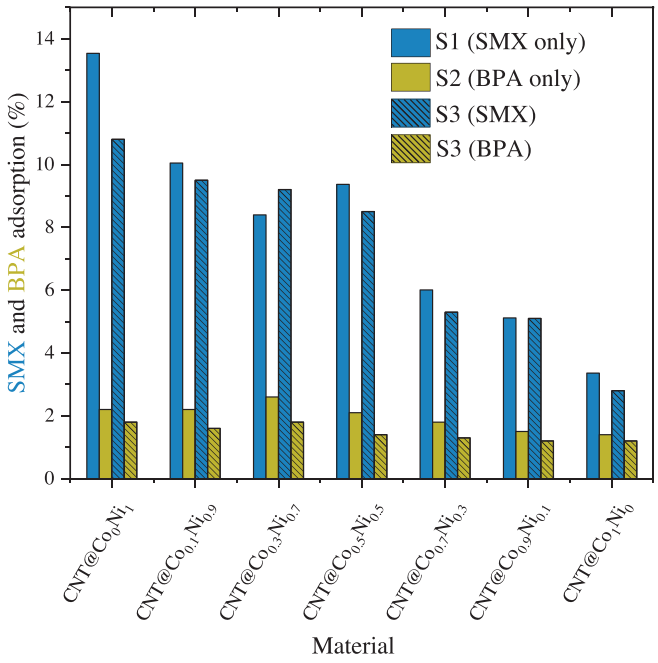

Figure 4. Adsorption results obtained after 8 h for systems S1 (SMX), S2 (BPA), and S3 (SMX and BPA). Operating conditions: T = 80 °C, pH_0 = 3.5, C_{ADS} = 2.5 g L^{-1}, $C_{SMX,0}$ = 10 mg L^{-1}, $C_{BPA,0}$ = 10 mg L^{-1}.

whereas in system S2 (BPA only), PFO was the best fit. In the multi-component system (S3), the PSO model again provided the best fit for H_2O_2 decomposition. For pollutant degradation, the PSO model better described experimental concentration profiles in single-component experiments. However, in the multi-component system, PFO better represented SMX degradation, contrasting with the single-component results. Meanwhile, the PSO model continued to provide the best fit for BPA degradation in the multi-component system, consistent with its performance in the single-component system. The shift in SMX degradation kinetics from PSO in the single-component system to PFO in the multi-component system suggests potential interactions or competition between pollutants,affecting their degradation mechanisms. In contrast, the consistency of BPA degradation kinetics across single- and multi-component systems implies that the presence of other pollutants less influences its degradation mechanism.

Pure adsorption experiments were also performed under similar operating conditions to evaluate the pure removal of pollutants via this mechanism, and the results are shown in Figure 4.

The results obtained in pure adsorption experiments revealed that SMX has a higher affinity with the CNTs than BPA. SMX adsorption ranged from 3.3% to 13.5% in single-component adsorption (S1) and from 2.8% to 10.8% in multi-component adsorption (S3). BPA had about the same adsorption values in single-component (S2) and multi-component experiments (S3), ranging from 1.4% to 2.2% in S2 and from 1.2% to 1.8% in S3. The higher adsorption of SMX compared to BPA is attributed to the pollutant being in its cationic form at the acidic pH used in the experiment (BPA is mostly neutral since its pK_a is in the range 9.8–10.4[52]). In the cationic form, SMX has a higher interaction

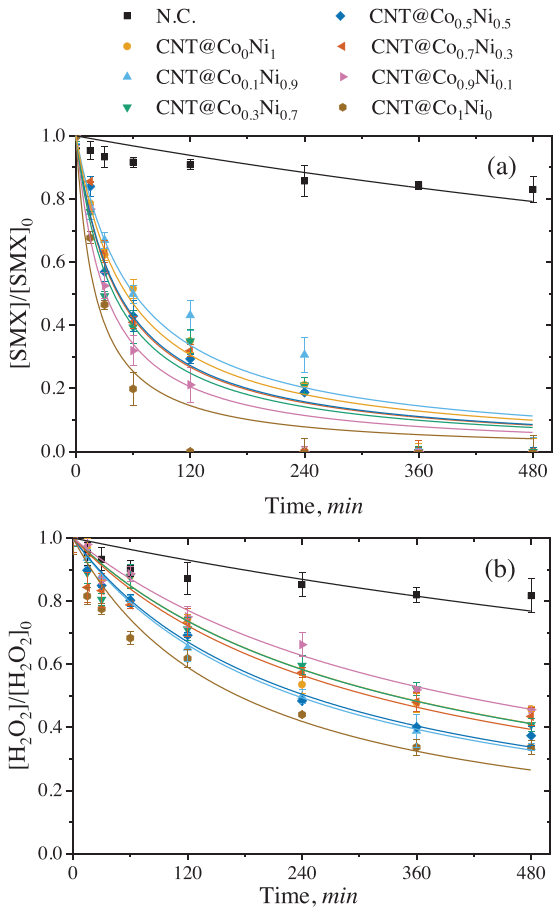

Figure 5. (a) SMX and (b) H_2O_2 normalized concentration during CWPO (system S1). Operating conditions: T = 80 °C, pH_0 = 3.5, C_{CAT} = 2.5 g L^{-1}, $C_{SMX,0}$ = 10 mg L^{-1}, $C_{H2O2,0}$ = 44.3 mg L^{-1}. Lines were obtained with PSO kinetic modelling. N. C.: noncatalytic.

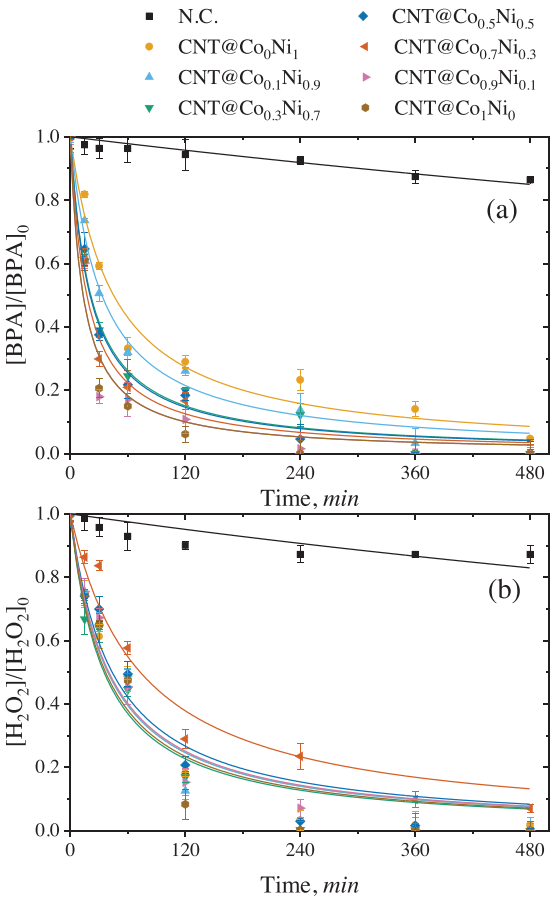

Figure 6. (a) BPA and (b) H_2O_2 normalized concentration during CWPO (system S2). Operating conditions: T = 80 °C, pH_0 = 3.5, C_{CAT} = 2.5 g L^{-1}, $C_{BPA,0}$ = 10 mg L^{-1}, $C_{H2O2,0}$ = 53.6 mg L^{-1}. Lines were obtained with PSO kinetic modelling. N.C.: noncatalytic.

with the material surface, favoring the adsorption process.[53,54] Specifically, SMX can engage in π-π interactions with the aromatic structure of the CNTs. In addition, the SMX molecule is smaller than BPA, allowing the compound to access the porosity of the carbon material more efficiently. The SMX adsorption also revealed a strong dependency on the surface area of the materials, the coefficient of determination (r^2) being 0.8 in single and 0.6 in multi-component experiments (linear regression). The lower adsorption observed for both pollutants in the multi-component experiment is related to the competition for the active sites.

The results obtained in the CWPO experiments will be discussed in each system separately, starting with the results obtained in system S1 for the degradation of SMX shown in Figure 5.

The results demonstrated that all materials tested had high catalytic activity toward the degradation of SMX in batch experiments since all materials were able to degrade SMX completely within 6 h of reaction (360 min). H_2O_2 decomposition was not complete after 8 h (480 min), which can be related to a possible complex interaction between the oxidant source and the catalyst surface due to SMX adsorption. As shown in Figure 4, CNTs adsorb SMX, which can interfere with H_2O_2 decomposition into hydroxyl radicals. On the other hand, the presence of SMX at the catalyst's surface can speed up its degradation when hydroxyl radicals are formed, which can explain the complete degradation of the pollutant with all materials in 6 h of reaction. The contribution of the adsorption in the process will also be accounted for in a later discussion of the results obtained in desorption experiments to evaluate if the pollutants adsorbed are being degraded. Regarding the different performances of the CNTs, the results indicate a tendency of increased activity with a higher content of cobalt in their structure, which can be related to the higher activity of this metal toward H_2O_2 decomposition compared to nickel.[55,56] In this context, the best catalyst, CNT@Co_1Ni_0, achieved complete degradation of SMX within 2 h of reaction, whereas its counterpart, CNT@Co_0Ni_1, was able to degrade completely the pollutant within 6 h (360 min).

The results obtained for BPA degradation in S2 (only BPA) are shown in Figure 6.

The materials also demonstrated high catalytic activity for the degradation of BPA, achieving complete abatement of the pollutant within 4–8 h (240–480 min), depending on the catalyst. The decomposition of H_2O_2 was more pronounced in these experiments than in S1 (experiment with only SMX). Considering the lower adsorption capacity of the CNTs toward BPA, the

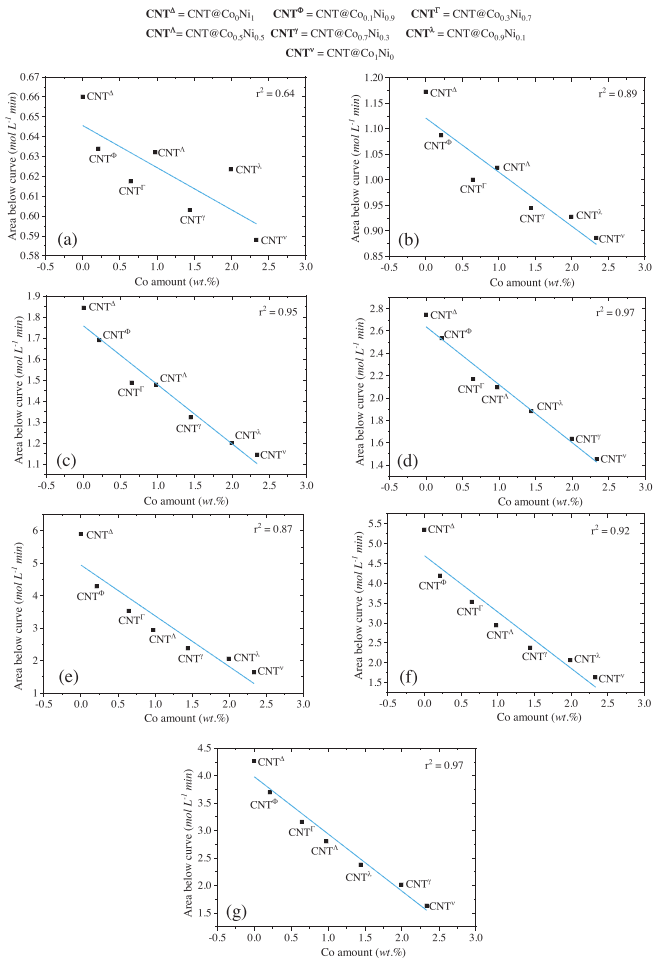

Figure 7. Linear regression obtained comparing the amount of Co in the CNTs with the cumulative area below the BPA decay curve in the system S2 (CWPO of BPA only) in times (a) 15, (b) 30, (c) 60, (d) 120, (e) 240, (f) 360, and (g) 480 min.

catalyst surface was more available for interactions with H_2O_2, enabling a higher decomposition of the oxidant source. The dependency between the Co amount in the catalyst and activity is more pronounced in this system than in S1, with the same tendency observed before ($CNT@Co_1Ni_0$ is the best and $CNT@Co_0Ni_1$ is the worst). For instance, considering the pollutant abatement over time, the area below the curve can be calculated to compare the different catalysts used in the process. The best catalyst will be the one with the smallest area below the curve, considering that the material was faster in the degradation of the model pollutant. For instance, it is also possible to go beyond and compare the different amounts of Co in the materials with the area below the curve in different reaction times to understand if, indeed, the different amounts of metals in the CNTs are making any difference in the process. Figure 7 shows the result obtained upon comparing the amount of Co and the integration results of the curve $C(t)$ versus t.

The results reveal a strong correlation between the amount of Co and the area below the curve, proving what could already be observed in Figure 6. The higher amount of Co, leading to the smallest area below the curve, indicates that more Co in the catalysts results in a higher efficiency since, in those cases, the decay of the pollutant concentration is more accentuated.

System S2 is ideal for this comparison due to the negligible BPA adsorption, showing that the sharpening concentration decrease is probably coming from degradation by CWPO and not from the adsorption process. In the early reaction stage ($t < 30$ min), pollutant, oxidant source, and catalyst interactions are not yet stable. This explains the weaker correlation between the amount of Co in the catalysts and the reaction performance. After this period, the correlations remained higher than 0.9 for all reaction times. The same process performed in system S1 yields lower coefficients of determination, precisely 0.02, 0.17, 0.53, 0.72, 0.82, 0.86, and 0.86 for reaction times of 15, 30, 60, 120, 240, 360, and 480 min, respectively. Despite being smaller, the values are still representative of the correlation between Co amount and catalytic efficiency after the initial reaction period ($t < 30$ min).

Finally, the results obtained for the multi-component system (S3) are shown in Figure 8. The noncatalytic experiment in a multi-component system was similar to single-component systems. All catalysts demonstrated higher degradation in the multi-component system, surpassing the BPA and SMX degradation and H_2O_2 decomposition compared to the single-component system. Both pollutants were removed within smaller time intervals, comparing the multi-component system with the single-component ones. For instance, in S1, complete degradation of SMX within 2–6 h of reaction was verified, whereas in S3, the pollutant was completely degraded within 0.5–4 h of reaction. The same behavior was observed for BPA, degraded within 4–8 h in S2 and 2–6 h in S3.

The faster removal of both pollutants in S3 under conditions similar to those of the single-component systems can be related to the higher proximity between molecules in the S3 system due to the higher concentration of molecules than in the single-component systems. This higher proximity increases the interaction between pollutants and the hydroxyl radicals (in excess) formed during the reaction. Previous reported works discuss improved degradation efficiencies in heterogeneous Fenton reactions when comparing single-component and multi-component systems.[57,58] This improvement is primarily attributed to synergistic effects among pollutants and catalysts, such as enhanced reactive oxygen species (ROS) generation and diverse reaction pathways.[59] However, while competition for active sites plays a role, it does not always lead to synergy and can sometimes hinder efficiency depending on pollutant reactivity and adsorption dynamics.[59] The tendency of increased degradation of the pollutants with increasing Co in the catalyst was also verified in this system. One difference that can be observed in terms of H_2O_2 decomposition, comparing the multi-component system with the single SXM one (S1), is the higher H_2O_2 decomposition in S3 than in S1. Considering the results obtained for adsorption in S3, it is possible to observe that SMX adsorption in this system was lower than in S1, which can lead to more active sites available for H_2O_2 decomposition.

The correlation between BPA degradation efficiency and the amount of Co in the catalyst is weak in the multi-component system. Specifically, the coefficients of determination are 0.56, 0.01, 0.46, 0.41, 0.45, 0.55, and 0.56 for times of 15, 30, 60,

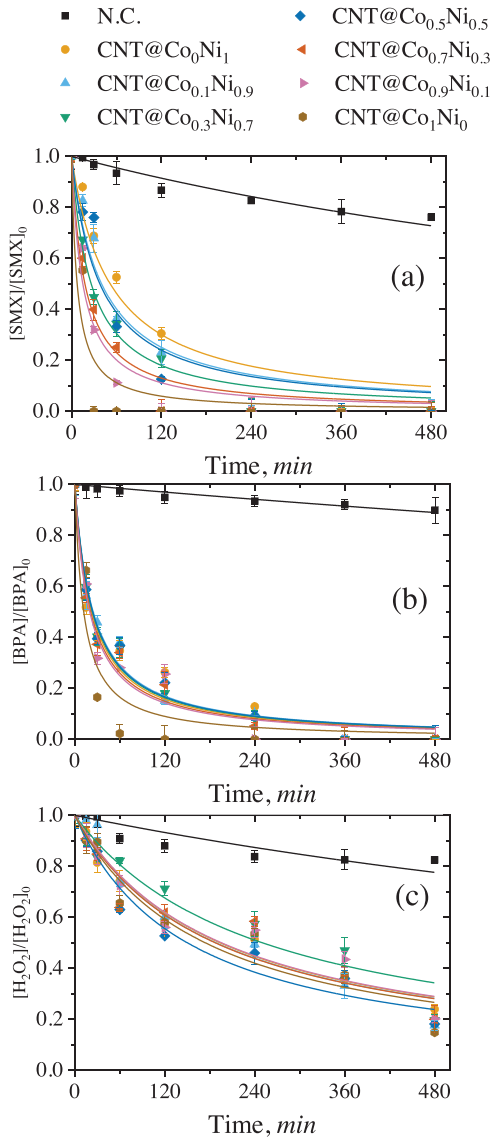

Figure 8. (a) SMX, (b) BPA, and (c) H_2O_2 normalized concentration during CWPO (system S3). Operating conditions: T = 80 °C, pH_0 = 3.5, C_{CAT} = 2.5 g L^{-1}, $C_{SMX,0}$ = 10 mg L^{-1}, $C_{BPA,0}$ = 10 mg L^{-1}, $C_{H2O2,0}$ = 98.01 mg L^{-1}. Lines were obtained with PSO kinetic modelling. N.C.: noncatalytic.

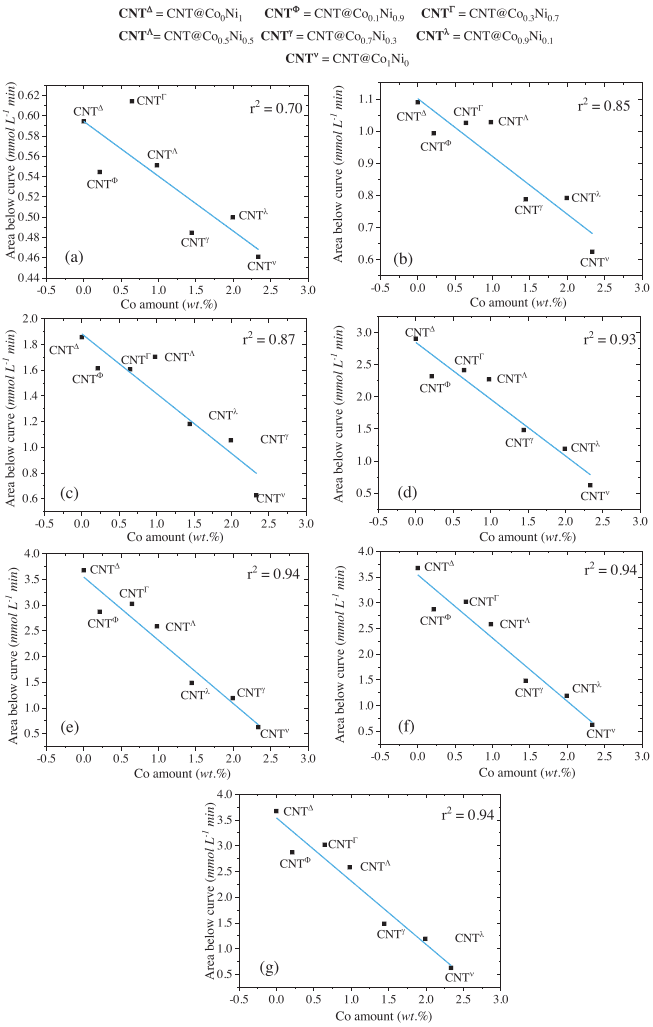

Figure 9. Linear regression obtained comparing the amount of Co in the CNTs with the cumulative area below the SMX decay curve in system S3 (CWPO of SMX and BPA) in times (a) 15, (b) 30, (c) 60, (d) 120, (e) 240, (f) 360, and (g) 480 min.

120, 240, 360, and 480 min, respectively. On the other hand, the results obtained for SMX are surprisingly better than in a single-component system, as can be observed in Figure 9.

The results obtained with this analysis suggest that in the single-component system, SMX degradation is governed by the adsorption of the pollutant in the CNTs, which complicates the access of the active sites to H_2O_2 molecules. In this situation, the amount of Co in the material will not significantly impact the process due to the hindered interaction between the catalyst and H_2O_2. In system S2, with BPA, the catalyst surface plays an important role, with degradations correlating once again with the amount of Co in the catalyst. Finally, in the last system (S3), the presence of both pollutants competing for active sites with H_2O_2 complicates the adsorption process, which was already demonstrated in Figure 4. However, due to the stronger affinity between SMX and the CNTs, the pollutant is more likely to be closer to the catalyst surface than BPA, which explains the higher dependency between the catalyst activity measured in terms of the presence of Co and the degradation of SMX in S3. Since SMX is closer to the surface and degraded more easily, BPA degradation in this scenario will be more stochastic than in a single-component system. Comparing the catalyst surface with H_2O_2 decomposition would not result in significant results due to the interaction between H_2O_2 and all the components in the system, not only with the catalyst.

After evaluating the performance of the catalysts in the systems studied here, it is also essential to consider the metal leaching during the reactions and the desorption experiment results to understand which catalyst has the highest potential for the degradation of organic pollutants via CWPO. The results obtained for the desorption essays and metal leaching during the experiments are shown in Figure 10a,b, respectively.

The results shown in Figure 10a refer to the desorption experiments performed on materials recovered after the adsorption process, which were performed to validate the experimental pro-

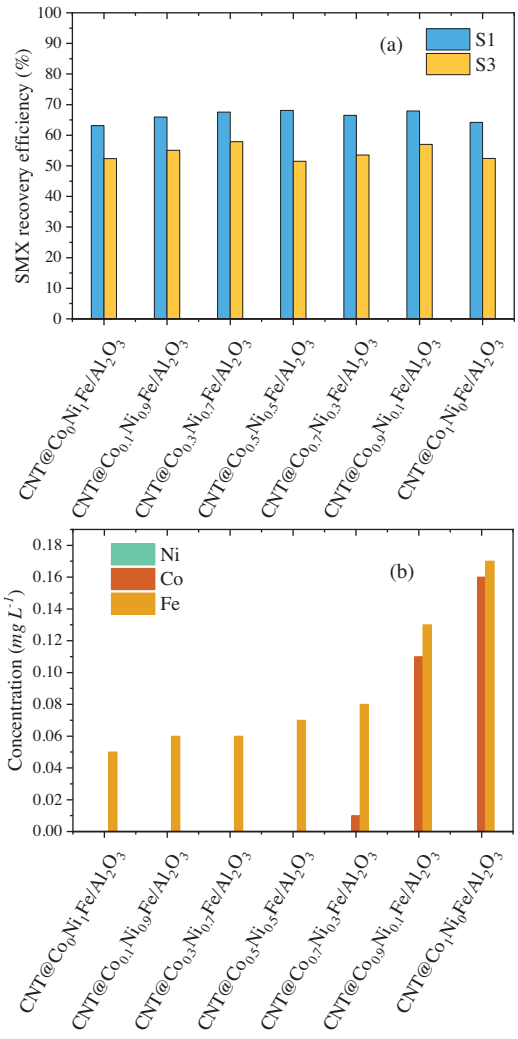

Figure 10. Results obtained on (a) pollutant desorption experiments using materials recovered from pure adsorption and CWPO experiments and (b) metal leaching measured at the end of CWPO.

cedure and evaluate the recovery efficiency. It was possible to recover at least 50% SMX in all cases. No BPA was recovered from S2 or S3 from the materials after the adsorption process, and no pollutant was recovered after the CWPO process. The lack of pollutant recovery after CWPO, at least in the case of SMX, could indicate that some adsorbed pollutants might have been degraded. Moreover, the results of metal leaching (Figure 10b) revealed that no Ni leaching was identified from all materials, and Co and Fe leaching occurred at different levels. No Co leaching was identified in materials prepared using a CVD catalyst with less than 50 wt.% of Co phase in the active phase (CNT@Co_0Ni_1, CNT@$Co_{0.1}Ni_{0.9}$, and CNT@$Co_{0.3}Ni_{0.7}$). All other materials had leaching that increased with increasing Co amount. Iron leaching was observed for all materials, but the leaching increased significantly when Co leaching was also identified.

Considering the results obtained in the synthesis procedure (CNTs yield), the catalytic activity of the CNTs, and the results related to leaching, the material performing better would be CNT@$Co_{0.7}Ni_{0.3}$. This material has a balanced yield in the synthesis procedure and significant catalytic activity in the process, without presenting substantial leaching of the active phase.

All catalysts were recovered at the end of the experiments, and the best-performing material (CNT@$Co_{0.7}Ni_{0.3}$) was reused in the multi-component system. The results shown in Figure S10 revealed that the CNT lost some catalytic activity from the first to the second use, with about 5% less H_2O_2 conversion and ca. 10% BPA and SMX degradation after 8 h of reaction. The loss of activity after the first use can be a consequence of the partial surface oxidation of the carbon phase due to interaction with H_2O_2 and metal leaching, detected in the first use. Previous reports have observed changes in the catalytic activity of carbon-based materials during reutilization runs related to surface oxidation.[31] However, the third use revealed the same results obtained in the second cycle, confirming that the catalyst was stable from the second to the third runs. No metal leaching was observed in the second and third reuse experiments, which suggests that the main contribution to the catalytic activity comes from the heterogeneous catalyst and not from a homogeneous Fenton reaction due to metal leaching. The role of the solid catalyst in pollutant degradation was confirmed through an additional experiment using a fresh catalyst. In this test, the catalyst was removed from the reaction medium by filtration after 30 min, and the reaction was allowed to proceed without it. As shown in Figure S11, the conversion of H_2O_2 and the degradation of SMX and BPA ceased immediately after the catalyst was removed.

The catalytic and structural performance of the Co—Ni-based CNTs prepared in the present work can be meaningfully compared with other materials reported in the literature. For instance, Alamro et al.[60] prepared $NiFe_2O_4$/CNT electrocatalysts via sol-gel for electrooxidation of ethylene glycol, showing high catalytic activity due to synergistic interaction between CNTs and spinel oxides, although the application was electrochemical rather than oxidative degradation of pollutants in aqueous media. Shokrgozar et al.[61] synthesized $NiCo_2O_4$/multi-walled CNTs nanocomposites and demonstrated improved photocatalytic degradation of Reactive Red 120 dye under UV radiation, in which CNTs enhanced both stability and catalytic performance. Similarly, Lu et al.[62] developed $Co_xNi_{1-x}Fe_2O_4$/multi-walled CNT composites for photocatalytic degradation of methylene blue, showing the benefit of combining ferrites with CNTs for reusable and efficient H_2O_2-activated degradation systems. Compared to these studies, our materials uniquely combine controlled cobalt–nickel ferrite ratios, CNTs synthesized directly from plastic waste, and application in CWPO, allowing both enhanced H_2O_2 activation and a sustainable synthesis route.

4. Conclusion

This study successfully demonstrates the synthesis of CNTs from model PSWs using mixed cobalt-nickel-iron oxide catalysts via CVD and their application in CWPO for pollutant degradation. The findings underscore the significant influence of catalyst composition on the yield, morphology, and catalytic performance of the CNTs. Higher cobalt content led to thicker CNT walls and

improved catalytic activity, particularly in BPA degradation, but was also associated with increased metal leaching. The most effective catalyst, CNT@$Co_{0.7}Ni_{0.3}$, achieved an optimal balance between CNT yield, catalytic efficiency, and stability. Beyond these immediate findings, the study provides critical insights into future research. One key consideration is the long-term stability and reusability of CNT-based catalysts in continuous wastewater treatment systems. While cobalt-enriched CNTs demonstrated superior activity, further efforts should focus on mitigating metal leaching to ensure sustained performance and minimize environmental impact.

Another important avenue for exploration is the scalability of this process. While the synthesis of CVD-based CNTs from PSWs has been demonstrated at the laboratory scale, industrial implementation requires further feedstock processing, reactor design, and energy efficiency optimization. Additionally, the potential applications of these CNTs in broader catalytic processes, such as electrochemical oxidation or hybrid advanced oxidation techniques, remain largely unexplored.

Overall, this study highlights the feasibility of converting polymers into functional CNT catalysts with significant environmental benefits. This approach can contribute to sustainable wastewater management and pollution control strategies with further refinement and industrial adaptation.

5. Experimental Section

5.1. Reagents and Materials

The precursors used in the preparation of the CNTs, HDPE (melt index 2.2 g (10 min)$^{-1}$), LDPE (average Mw ~ 35000 g mol^{-1}, average Mn ~7700), and PP (average Mw ~250000 g mol^{-1}, average Mn ~67,000), were supplied by Sigma-Aldrich. For the preparation of the Ni/Co ferrites CVD catalysts, iron (III) chloride hexahydrate (97 wt.%), nickel (II) chloride hexahydrate (97 wt.%), and cobalt (II) chloride (98 wt.%) supplied by Fisher Chemicals were used. Alumina was supplied by Alfa Aesar.

The CWPO batch experiments performed with the materials prepared using different CVD metal catalysts were carried out using SMX (98 wt.%) and BPA (98 wt.%), supplied by Supelco. Hydrogen peroxide (30 w/v%) was supplied by Alfa Aesar. For analytical measurements, formic acid (95 v/v%), sodium sulfite anhydrous (98 wt.%), and titanium (IV) oxysulfate (99.99 wt.% metal basis, ca. 15 wt.% solution in dilute sulfuric acid) were provided by Fisher Chemical. All chemicals were used as received. Ultrapure and distilled water have been used during this work for the preparation of solutions and washing procedures.

5.2. Synthesis of the CVD Catalysts

The Ni/Co based CVD catalysts were prepared following a methodology similar to that reported in the previous works.[6] In brief, the materials were all prepared to achieve 15% of the metal phase supported on alumina. The Co/Ni mixed ferrites were named $Co_xNi_{1-x}Fe/Al_2O_3$, depending on the relative molar amount of Co and Ni in their formulation.

For the synthesis procedure, M^{2+} salts (*e.g.*, Ni^{2+} and Co^{2+}) were dissolved in ethanol, while M^{3+} salts (e.g., Fe^{3+}) were dissolved in ethanediol. In this case, the same ratio should be used in all experiments, $M^{3+}/M^{2+} = 2$. The M^{2+} solution is heated to its boiling point, and the M^{3+} solution is heated to 60 °C for 5 min, then cooled in an ice bath to control the reaction between anions and the solvent. Once the M^{3+} solution reaches the room temperature, the two solutions are combined with alumina (5.67 g) and stirred at 60 °C for 2 h. Subsequently, the temperature is increased to 120 °C, continuously stirring for 4 h, until a dark-yellow gel forms. Finally, the temperature is raised to the boiling point of ethanediol (189 °C) to produce a dark-brown magnetic solid. The resulting precursor of ferrites is further processed in a vertical tubular furnace (ROS 50/250/12, Thermoconcept) for thermal treatment at 300 °C for 6 h and 600 °C for 3 h to remove organic residues from the synthesis. Table 4 brings all the materials prepared in this step, along with molar amounts of the reagents.

Table 4. CVD catalysts names and molar amounts used in the synthesis procedure.

CVD Catalyst	Ni^{2+}(mmol)	Co^{2+} (mmol)	Fe^{3+} (mmol)
Co_0NiFe/Al_2O_3	4	0	8
$Co_{0.1}N_{0.9}iFe/Al_2O_3$	3.96	0.4	8
$Co_{0.3}Ni_{0.7}Fe/Al_2O_3$	2.8	1.2	8
$Co_{0.5}Ni_{0.5}Fe/Al_2O_3$	2	2	8
$Co_{0.7}Ni_{0.3}Fe/Al_2O_3$	1.2	2.8	8
$Co_{0.9}Ni_{0.1}Fe/Al_2O_3$	0.4	3.96	8
$CoNi_0Fe/Al_2O_3$	0	4	8

5.3. Synthesis of the Carbon Nanotubes (CNTs)

The CNTs were synthesized by chemical vapor deposition (CVD), following a methodology similar to that reported in a previous work,[6] and using the one-chamber reactor illustrated in Figure S12. For the synthesis, the upper crucible (polymer cracking zone) was loaded with 5 g of MIX (2 g PP, 1.25 g HDPE, and 1.75 g LDPE), and the lower crucible (CVD zone) was loaded with 1 g of a Ni/Co CVD catalyst. The polymeric amounts used in MIX were calculated from the real percentage of polymers per type found in PSW.[63] The CVD zone of the reactor was set to 850 °C, and the polymer cracking zone was set to 450 °C. The synthesis procedure was performed for 90 min under an N_2 flow of 50 mL min^{-1}. The recovered material was washed with distilled water at room temperature to remove CVD metal catalyst phases that were deactivated during the synthesis and are not within the CNT structure. The materials were named as CNT@Co_0Ni, CNT@$Co_{0.1}Ni_{0.9}$, CNT@$Co_{0.3}Ni_{0.7}$, CNT@$Co_{0.5}Ni_{0.5}$, CNT@$Co_{0.7}Ni_{0.3}$, CNT@$Co_{0.9}Ni_{0.1}$, and CNT@$CoNi_0$, prepared with Co_0NiFe/Al_2O_3, $Co_{0.1}Ni_{0.9}Fe/Al_2O_3$, $Co_{0.3}Ni_{0.7}Fe/Al_2O_3$, $Co_{0.5}Ni_{0.5}Fe/Al_2O_3$, $Co_{0.7}Ni_{0.3}Fe/Al_2O_3$, $Co_{0.9}Ni_{0.1}Fe/Al_2O_3$, and $CoNi_0Fe/Al_2O_3$, respectively.

The synthesis yield was determined considering the total carbon content from model MIX (average 85.6 wt.% content determined theoretically). Considering the total carbon in MIX, the yield was determined according to Equation (1),

$$\text{Yield} = \frac{m_{rec} - m_{CVD}}{m_C} \times 100 \quad (1)$$

in which m_{rec} is the mass of material recovered from the oven, m_{CVD} is the mass of CVD catalyst used in the synthesis procedure, and m_C is the mass of carbon in MIX, considering the theoretical amount of carbon.

5.4. Characterization Techniques

The materials were characterized based on the methodologies described in previous works.[64,65] The metal content in the CVD catalyst was determined by digesting 100 mg of sample in 5 mL of aqua regia for 72 h at 105 °C in a digesting block (Hanna Instruments, HI839800 COD reactor). For the CNTs, the samples were previously burnt in a muffle furnace for 24 h at 800 °C to eliminate the organic content. The ashes were digested following the same procedure reported for the CVD catalysts. The resulting liquid was analyzed by atomic absorption to determine the metal content. The correlation between Co and Ni metals detected in liquid samples and Co and Ni contents was determined based on the XRD semi-quantitative analysis for CVD catalysts. For the CNTs, the values calculated are based on the sole Co and Ni content from the materials. Selected CVD catalyst samples (Co_0Ni_1Fe/Al_2O_3, $Co_{0.5}Ni_{0.5}Fe/Al_2O_3$, and Co_1Ni_0Fe/Al_2O_3) were characterized by X-Ray diffraction (XRD) to perform crystalline phase identification. A PANalytical X'Pert Pro diffractometer equipped with an X'Celerator detector and secondary monochromator in $\theta/2\theta$ Bragg-Brentano geometry was used in the analysis, at room temperature. The measurements were carried out using 40 kV and 30 mA, a CuKα radiation ($\lambda\alpha_1 = 1.54060$ Å and $\lambda\alpha_2 = 1.54443$ Å), 0.017°/ step, 100 s/step, in a 10–80° 2θ angular range. Data processing was performed using the software X'Pert HighScore Plus with reference cards from the Crystallography Open Database.

Briefly, textural properties of all samples were characterized by analysis of N_2 adsorption-desorption isotherms at −196 °C obtained in a Quantachrome NOVATOUCH LX^4 adsorption analyzer equipped with long cells with a bulb and outer diameter of 9 mm. The specific surface area was determined using the BET method (S_{BET}) available in the Quantachrome TouchWin Software (version 1.21) in the range of $p/p^0 = 0.05$–0.35, and the total pore volume (V_T) was considered at $p/p^0 = 0.98$.[66] Before analysis, all samples were degasified at 120 °C for 6 h, as recommended by IUPAC.

Thermogravimetric analysis (TGA) was performed on a simultaneous TGA-DSC thermobalance (TGA-DCS1, Mettler-Toledo, S.A.E.) using a flow rate of 100 mL min^{-1} of air and a heating rate of 10 °C min^{-1}. The elemental analysis (CHNS) was carried out in a Flash 2000 analyzer (Thermo Fisher Scientific, Massachusetts, USA), which was provided with a thermal conductivity detector (TCD). The Raman spectra were directly measured on the carbon materials using an apparatus Alpha 300 from WiTec, Germany, equipped with a monochromatic laser of 635 nm wavelength. This instrument is outfitted with a high-resolution germanium array detector and operates with an Nd-YAG laser source at 632 nm.

The transmission electron microscopy (TEM) images were obtained using a double-corrected FEI Titan G3 Cubed Themis, operated at 200 kV. The images recorded by TEM were processed with ImageJ. The images recorded by TEM were processed in ImageJ, if applicable. Wall counting was performed using the *Plot Profile* tool from ImageJ, enabling pixel intensity visualization in a straight line. This tool ensures proper counting of the walls of the CNTs, which can be a complicated task. The diameter was measured by counting as many CNTs as possible in a single image, repeating the process with 3 images for each sample to ensure reproducibility.

5.5. CWPO Batch Experiments

The CNTs were tested as catalysts (2.5 g L^{-1} of catalyst load) in the CWPO under the same operating conditions selected in previous studies.[1] In brief, the catalyst concentration was set to 2.5 g L^{-1}, the temperature was kept at 80 °C, and the initial pH was adjusted to 3.5. Those conditions ensure the efficient decomposition of H_2O_2 into hydroxyl radicals.[23] The tests were performed in three different systems: the first contained only SMX ($C_{SMX,0} = 10$ mg L^{-1}), the second system contained only BPA ($C_{BPA,0} = 10$ mg L^{-1}), and the last was a multi-component system containing both pollutants, each at 10 mg L^{-1} concentration. The stoichiometric concentration of H_2O_2 for complete mineralization was used in all experiments, and calculated based on Equation (2) (SMX) and Equation (3) (BPA),

$$C_{10}H_{11}N_3O_3S + 33H_2O_2 \rightarrow 10CO_2 + 36H_2O + H_2SO_4 + 3HNO_3 \quad (2)$$

$$C_{15}H_{16}O_2 + 36H_2O_2 \rightarrow 15CO_2 + 44H_2O \quad (3)$$

The experimental procedure was the same in all experiments. Once the pollutant and oxidant source were homogenized in a two-necked round-bottom flask equipped with a condenser, the catalyst was poured into the liquid to reach the desired concentration. The first sampling was performed moments before adding the catalyst to the reaction media. Samples were periodically collected at selected reaction times of 15, 30, 60, 120, 240, 360, and 480 min to monitor pollutants and H_2O_2 concentrations throughout time. The samples collected for H_2O_2 concentration analysis were soon processed, and other samples used for pollutant concentration determination were stored in a fridge with added Na_2SO_3, to consume the H_2O_2 remaining in the sample and stop the reaction. Adsorption was conducted in the absence of the oxidant under the same operating conditions as considered in the CWPO experiments. In addition, a noncatalytic experiment was conducted without a catalyst (N.C.). All the materials were recovered, washed with distilled water to remove possible reagents, and dried overnight after the end of the reaction. The best catalyst recovered from the multi-component system was used in the other 2 cycles to confirm the stability of the catalyst. In addition, an additional experiment was carried out to confirm that the catalytic activity originated from the solid catalyst. The procedure involved removing the catalyst by filtration through 0.45 µm PTFE syringe filter, after which the filtrate was transferred to a clean reaction vessel. The reaction was allowed to proceed under identical conditions, with hydrogen peroxide and pollutant concentrations monitored at the same time intervals as in the original catalytic experiments. This control was performed using the catalyst (fresh) that exhibited the highest catalytic activity.

Desorption assays were conducted using the materials recovered from adsorption and oxidation experiments. The procedure followed optimized conditions and solvents for micropollutant desorption from carbonaceous materials.[25] Specifically, the recovered samples of CNTs were washed with 2 mL of distilled water to remove unadsorbed pollutants. Then, 30 mg of the washed samples were stirred in 20 mL of an aqueous solution containing 0.1 M NaOH and 20 v/v% absolute ethanol for 6 h at room temperature. After desorption, the liquid phase was filtered and stored for further analysis. The amount of pollutants desorbed from the materials was calculated using Equation (4),

$$C_{pol,des} = \frac{C_{pol} \cdot V}{m_{ads}} \quad (4)$$

in which C_{pol} represents the SMX or BPA concentration (mg L^{-1}), determined using HPLC, V the volume (L) of the aqueous extractant solution used for the experiment, and m_{ads} the mass (g) of material used in the experiment. The recovery efficiency was determined based on the maximum amount of pollutant adsorbed in the adsorption experiments.

5.6. Analytical Techniques and Statistical Treatment

The concentration of H_2O_2 and pollutants was followed in all experiments. H_2O_2 concentration was measured by adding 0.5 mL of sample into a 5 mL flask loaded with 0.1 mL $TiOSO_4$ and 1 mL H_2SO_4 (0.5 M). The resultant mixture was analyzed at 405 nm using a spectrophotometer T70 from PG Instruments Ltd. (Lutterworth, United Kingdom). The same procedure is reported in previous works from the group.[1,6,31]

The concentration of the pollutants (SMX and BPA) was measured using a Jasco HPLC system supplied with a UV–vis detector (UV-2075 Plus detector). For this determination, a BiPhenyl column (BPH 5 µm 150 × 2.1 mm) and an A: B mixture of acetonitrile (A) and ultrapure water acidified with 0.1 wt.% formic acid (B) were used. SMX and BPA were measured at the wavelength of 280 nm at a flow rate of 0.3 mL min^{-1} (PU-2089 Plus) using an isocratic composition of mobile phase A: B (10:90). Metal leaching at the end of the experiments was measured using atomic absorption spectroscopy (Varian SpectrAA 220).

All experiments, namely CWPO and adsorption, were performed in triplicate. The reported values are the average value, calculated according to Equation (5),

$$\overline{C}_t = \frac{\sum_{j=1}^{n} C_j}{n} \tag{5}$$

in which $\overline{C}_t$ is the average relative concentration of the parameter of interest (SMX, BPA, or H_2O_2) at time t, C_j is the concentration in run j for time t, and n is the total number of experimental runs (n = 3). The standard deviation (s_t) was calculated according to Equation (6),

$$s_t = \sqrt{\sum_{j=1}^{n} \frac{(C_j - \overline{C}_t)^2}{n-1}} \tag{6}$$

in which C_j is the relative concentration in time t for each run j, $\overline{C}_t$ is the average concentration in time t (calculated by Equation 3), and n is the total number of experimental runs. The standard deviation was below ca. 5% for all experiments.

5.7. Kinetic Modelling

The kinetic modelling of the degradation of pollutants and decomposition of H_2O_2 during the reaction was performed considering previous works dealing with reaction kinetics related to heterogeneous Fenton studies.[67] In brief, pseudo-first-order (PFO) and pseudo-second-order (PSO) models were evaluated for pollutants (SMX and BPA) and H_2O_2 over the reactions in the three systems studied. Table S4 presents the detailed models and equations. For the kinetic modelling, all concentrations were used in mM, and reaction times in minutes. Initial conditions to solve the equations were C_{SMX} = 39.5 µmol L^{-1}, C_{BPA} = 43.8 µmol L^{-1} in single- and multi-component systems, and C_{H2O2} = 1381.89 µmol L^{-1} in system S1, C_{H2O2} = 2120.87 µmol L^{-1} in system S2, and C_{H2O2} = 2736.88 µmol L^{-1} in system S3. The numerical integration was solved using the SciPy (*v.* 1.10.1) Python package to minimize the sum of the squared errors based on the experimental concentration of the compounds of interest, according to Equation S1. The coefficient of determination was also calculated for all models studied according to Equation S2.

Acknowledgements

This work was financially supported by national funds through FCT/MCTES (PIDDAC): CeDRI, UIDB/05757/2020 (DOI: 10.54499/UIDB/05757/2020) and UIDP/05757/2020 (DOI: 10.54499/UIDB/05757/2020); CIMO, UIDB/00690/2020 (DOI: 10.54499/UIDB/00690/2020) and UIDP/00690/2020 (DOI: 10.54499/UIDP/00690/2020); SusTEC, LA/P/0007/2020 (DOI: 10.54499/LA/P/0007/2020). This work was also financially supported by: UID/50020 of LSRE-LCM–Laboratory of Separation and Reaction Engineering–Laboratory of Catalysis and Materials–funded by Fundação para a Ciência e a Tecnologia, I.P. /MCTES through national funds; and ALiCE, LA/P/0045/2020 (DOI: 10.54499/LA/P/0045/2020). Fernanda F. Roman acknowledges the national funding by FCT and the European Social Fund, FSE, through the individual research grant SFRH/BD/143224/2019. Adriano S. Silva was supported by the doctoral Grant SFRH/BD/151346/2021 and Ana Paula Ferreira by PRT/BD/153090/2021, financed by FCT with funds from NORTE2020, under MIT Portugal Program. Jose L. Diaz De Tuesta acknowledges the financial support through the program of *Atracción al Talento* of *Comunidad de Madrid* (Spain) for the individual research grant and project 2022-T1/AMB-23946 and through the program *Consolidación Investigadora 2024* (CNS2024-154264) supported from *Agencia Estatal de Investigación* (Spain). The authors are also grateful for the finantial support provided by Sociedade Ponto Verde for the project "Estudo técnico-económico para a valorização de resíduos de embalagens plásticas na produção de nanotubos de carbono."

Conflict of Interests

The authors declare no conflict of interest.

Data Availability Statement

Data will be made available upon request.

Keywords: Carbon material · Carbon nanotubes · CWPO · Multi-component · Wastewater treatment

[1] F. F. Roman, A. S. Silva, J. L. Diaz de Tuesta, A. P. Baldo, J. P. M. Lopes, G. Gonçalves, A. I. Pereira, P. Praça, A. M. T. Silva, J. L. Faria, M. Bañobre-López, H. T. Gomes, *J. Environ. Chem. Eng.* **2025**, *13*, 115206.
[2] S. Serranti, A. Gargiulo, G. Bonifazi, *Waste Manage.* **2011**, *31*, 2217–2227.
[3] C. Abdy, Y. Zhang, J. Wang, Y. Yang, I. Artamendi, B. Allen, *Resour. Conserv. Recycl.* **2022**, *180*, 106213.
[4] O. Kökkılıç, S. Mohammadi-Jam, P. Chu, C. Marion, Y. Yang, K. E. Waters, *Adv. Colloid Interface Sci.* **2022**, *308*, 102769.
[5] G. Lopez, M. Artetxe, M. Amutio, J. Bilbao, M. Olazar, *Renewable Sustainable Energy Rev.* **2017**, *73*, 346–368.
[6] J. L. Diaz de Tuesta, A. S. Silva, F. F. Roman, L. F. Sanches, F. A. da Silva, A. I. Pereira, A. M. T. Silva, J. L. Faria, H. T. Gomes, *Catal. Today* **2023**, *419*, 114162.
[7] A. Yahyazadeh, B. Khoshandam, *Results Phys.* **2017**, *7*, 3826–3837.
[8] G. P. Gakis, S. Termine, A. F. A. Trompeta, I. G. Aviziotis, C. A. Charitidis, *Chem. Eng. J.* **2022**, *445*, 136807.

[9] S. Suzuki, S. Mori, *Appl. Surf. Sci.* **2019**, *471*, 587–594.
[10] W. Henao, F. Cazaña, P. Tarifa, E. Romeo, N. Latorre, V. Sebastian, J. J. Delgado, A. Monzón, *Chem. Eng. J.* **2021**, *404*, 126103.
[11] J. C. Acomb, C. Wu, P. T. Williams, *Appl. Catal. B* **2016**, *180*, 497–510.
[12] E. V. Shlyakhova, N. F. Yudanov, Y. V. Shubin, L. I. Yudanova, L. G. Bulusheva, A. V. Okotrub, *Carbon N Y* **2009**, *47*, 1701–1707.
[13] A. Venkataraman, E. V. Amadi, Y. Chen, C. Papadopoulos, *Nanoscale Res. Lett.* **2019**, *14*, 220.
[14] X.-D. Wang, K. Vinodgopal, G.-P. Dai, in *Perspective of Carbon Nanotubes*, IntechOpen, Rijeka **2019**, Ch. 2..
[15] A. Szabó, E. Kecsenovity, Z. Pápa, T. Gyulavári, K. Németh, E. Horvath, K. Hernadi, *Sci. Rep.* **2017**, *7*, 9557.
[16] A. Yahyazadeh, S. Nanda, A. K. Dalai, *Reactions* **2024**, *5*, 429–451.
[17] H. Ago, K. Nakamura, N. Uehara, M. Tsuji, *J. Phys. Chem. B* **2004**, *108*, 18908–18915.
[18] N. M. Briggs, L. Barrett, E. C. Wegener, L. V. Herrera, L. A. Gomez, J. T. Miller, S. P. Crossley, *Nat. Commun.* **2018**, *9*, 3827.
[19] M. Vir Singh, A. Kumar Tiwari, R. Gupta, *ChemistrySelect* **2023**, *8*, e202204715.
[20] A. S. Silva, P. Z. Filho, A. P. Ferreira, F. F. Roman, A. P. Baldo, M. Rauhauser, J. L. Diaz de Tuesta, A. I. Pereira, A. M. T. Silva, J. M. T. Pietrobelli, M. S. Kalmakhanova, D. D. Snow, H. T. Gomes, *Chem. Eng. J. Adv.* **2025**, *21*, 100707.
[21] H. Ma, G. Wang, Z. Miao, X. Dong, X. Zhang, *Sep. Purif. Technol.* **2020**, *252*, 117479.
[22] A. Santos Silva, M. Seitovna Kalmakhanova, B. Kabykenovna Massalimova, J. G. Sgorlon, D. D. T. Jose Luis, H. T. Gomes, *Catalysts* **2019**, *9*, 705.
[23] A. S. Silva, F. F. Roman, R. S. Ribeiro, J. Garcia, H. T. Gomes, *Environ. Sci. Pollut. Res.* **2024**, *31*, 65208–65219.
[24] Y. Wu, H. Zhang, Y. Yan, *J. Environ. Manage.* **2020**, *270*, 110907.
[25] A. S. Silva, J. L. Diaz de Tuesta, A. Henrique, F. F. Roman, D. Omralinov, H. Steldinger, J. Gläsel, B. J. M. Etzold, J. A. C. Silva, A. M. T. Silva, A. I. Pereira, H. T. Gomes, *Chem. Eng. J.* **2024**, *499*, 156574.
[26] A. Gacem, S. Modi, V. K. Yadav, S. Islam, A. Patel, V. Dawane, M. Jameel, G. K. Inwati, S. Piplode, V. S. Solanki, A. Basnet, *J. Nanomater.* **2022**, *2022*, 7238602, https://doi.org/10.1155/2022/7238602.
[27] A. Boukhemkhem, K. Rida, A. H. Pizarro, C. B. Molina, J. J. Rodriguez, *Clay Miner.* **2019**, *54*, 67–73.
[28] X. Ou, H. Daly, X. Fan, S. Beaumont, S. Chansai, A. Garforth, S. Xu, C. Hardacre, *ACS Catal.* **2022**, *12*, 7598–7608.
[29] D. Liu, C. Shi, Y. Nie, W. Peng, Y. A. Ming, *Main Group Chem.* **2023**, *22*, 375–388.
[30] P. Nazari, O. Nouri, Z. Xie, S. R. Setayesh, Z. Wei, *J. Hazard. Mater.* **2021**, *417*, 126015.
[31] A. S. Silva, F. F. Roman, A. V. Dias, J. L. Diaz de Tuesta, A. Narcizo, A. P. F. da Silva, I. Çaha, F. L. Deepak, M. Bañobre-López, A. M. C. Ferrari, H. T. Gomes, *J. Environ. Chem. Eng.* **2023**, *11*, 110806.
[32] R. S. Ribeiro, A. M. T. Silva, J. L. Figueiredo, J. L. Faria, H. T. Gomes, *Catal. Today* **2017**, *296*, 66–75.
[33] H. Su, X. Huang, Z. Zhang, Y. Ye, D. Wang, *Biomass Bioenergy* **2025**, *193*, 107579.
[34] I. Martin-Gullon, J. Vera, J. A. Conesa, J. L. González, C. Merino, *Carbon NY* **2006**, *44*, 1572–1580.
[35] Y. D. Lim, A. V. Avramchuck, D. Grapov, C. W. Tan, B. K. Tay, S. Aditya, V. Labunov, *ACS Omega* **2017**, *2*, 6063–6071.
[36] A. Pancotti, D. P. Santos, D. O. Morais, M. V. de Barros Souza, D. R. Lima, V. A. Scalla Vulcani, A. Martins, R. Landers, A. Braoios, *SN Appl. Sci.* **2021**, *3*, 716.
[37] S. K. Sushant, N. J. Choudhari, S. Patil, M. K. Rendale, S. N. Mathad, A. T. Pathan, *Int. J. Self-Propag. High-Temp. Synth.* **2023**, *32*, 61–116.
[38] X. Zhao, X. Zhang, C. Gao, P. Wang, Y. He, D. Chu, W. Bai, *Appl. Phy. A.* **2025**, *131*, 196.
[39] N. Gupta, S. M. Gupta, & S. K. Sharma, *Carbon Lett.* **2019**, *29*, 419–447.
[40] M. M. Hussein, S. A. Saafan, H. F. Abosheiasha, D. Zhou, D. S. Klygach, M. G. Vakhitov, S. V. Trukhanov, A. V. Trukhanov, T. I. Zubar, K. A. Astapovich, H. M. H. Zakaly, M. A. Darwish, *RSC Adv.* **2023**, *13*, 26879–26891.
[41] K. Raji, C. B. Sobhan, in *Handbook of Carbon Nanotubes* (Eds: J. Abraham, S. Thomas, N. Kalarikkal), Springer International Publishing, Cham **2020**, pp. 1–30.
[42] S. Venkatesan, B. Visvalingam, G. Mannathusamy, V. Viswanathan, A. G. Rao, *Int. Nano Lett.* **2018**, *8*, 297–308.
[43] M. Mases, D. Jacobsson, D. Wahlqvist, M. Ek, H. Wiinikka, *Appl. Surf. Sci.* **2024**, *672*, 160755.
[44] A. Vignes, O. Dufaud, L. Perrin, D. Thomas, J. Bouillard, A. Janès, C. Vallières, *Chem. Eng. Sci.* **2009**, *64*, 4210–4221.
[45] F. F. Roman, J. L. Diaz de Tuesta, F. K. K. Sanches, A. S. Silva, P. Marin, B. F. Machado, P. Serp, M. Pedrosa, A. M. T. Silva, J. L. Faria, H. T. Gomes, *Catal. Today* **2023**, *420*, 114001.
[46] F. F. Roman, L. De Grande Piccinin, A. Santos Silva, J. L. Diaz De Tuesta, I. V. K. Freitas, A. Vieira, G. Gonçalves Lenzi, A. Manuel Tavares Silva, J. L. Faria, H. T. Gomes, *Catalysts* **2023**, *13*, 1259.
[47] E. J. Petersen, D. X. Flores-Cervantes, T. D. Bucheli, L. C. C. Elliott, J. A. Fagan, A. Gogos, S. Hanna, R. Kägi, E. Mansfield, A. R. M. Bustos, D. L. Plata, V. Reipa, P. Westerhoff, M. R. Winchester, *Environ. Sci. Technol.* **2016**, *50*, 4587–4605.
[48] Z. Lu, D. Li, C. Wang, X. Chen, W. Xia, *Diam. Relat. Mater.* **2020**, *108*, 107932.
[49] D. Yao, Y. Zhang, P. T. Williams, H. Yang, H. Chen, *Appl. Catal. B* **2018**, *221*, 584–597.
[50] M. Verma, S. S. Chauhan, S. K. Dhawan, V. Choudhary, *Compos. B Eng.* **2017**, *120*, 118–127.
[51] B. L. N. Krishna Sai, P. Tambe, *Adv. Ind. Eng. Polym. Res.* **2022**, *5*, 183–197.
[52] T. Vasiljevic, T. Harner, *Sci. Total Environ.* **2021**, *789*.
[53] D. Pirozzi, A. Latte, A. Yousuf, F. De Mastro, G. Brunetti, A. EL Hassanin, F. Sannino, *Nanomaterials* **2024**, *14*, 406.
[54] X. Liu, S. Lu, Y. Liu, W. Meng, B. Zheng, *RSC Adv.* **2017**, *7*, 50449–50458.
[55] J. Li, X. Li, J. Han, F. Meng, J. Jiang, J. Li, C. Xu, Y. Li, *Sci. Rep.* **2019**, *9*, 15820.
[56] X. Liang, Z. He, Y. Zhong, W. Tan, H. He, P. Yuan, J. Zhu, J. Zhang, *Colloids Surf. A Physicochem. Eng. Asp.* **2013**, *435*, 28–35.
[57] W. Tian, J. Lin, H. Zhang, X. Duan, H. Sun, H. Wang, S. Wang, *J. Hazard. Mater.* **2021**, *408*, 124459.
[58] F. E. Soetaredjo, S. P. Santoso, V. B. Lunardi, A. Kurniawan, H. Shuwanto, J. Lie, K. Foe, W. Irawaty, M. Yuliana, J. N. Putro, A. E. Angkawijaya, Y. H. Ju, S. Ismadji, *J. Mol. Liq.* **2022**, *347*, 117989.
[59] J. Song, L. Zhu, S. Yu, G. Li, D. Wang, *RSC Adv.* **2024**, *14*, 33489–33511.
[60] F. S. Alamro, M. A. Hefnawy, N. S. Al-Kadhi, A. M. Mostafa, M. M. Motawea, H. A. Ahmed, A. S. Alshomrany, S. S. Medany, *Heliyon* **2024**, *10*, e35791.
[61] A. Shokrgozar, K. Seifpanahi-Shabani, B. Mahmoodi, N. M. Mahmoodi, F. Khorasheh, M. Baghalha, *Desalin. Water Treat.* **2021**, *216*, 389–400.
[62] M. Lu, Y. Chang, X. H. Guan, G. S. Wang, *RSC Adv.* **2019**, *9*, 33806–33813.
[63] Plastics Europe Association of Plastics Manufacturers, *Plastics—The Facts 2021 An analysis of European Plastics Production, Demand and Waste Data*, Plastic Europe, Europe **2021**. https://plasticseurope.org/knowledge-hub/plastics-the-facts-2021/.
[64] A. S. Silva, J. L. Diaz De Tuesta, T. Sayuri Berberich, S. Delezuk Inglez, A. R. Bertão, I. Çaha, F. L. Deepak, M. Bañobre-López, H. T. Gomes, *Nanoscale* **2022**, *14*, 7220–7232.
[65] S. Moretto, A. S. Silva, J. L. Diaz de Tuesta, F. F. Roman, R. Cortesi, A. R. Bertão, M. Bañobre-López, M. Pedrosa, A. M. T. Silva, H. T. Gomes, *Mater. Today Chem.* **2023**, *33*, 101748.
[66] B. Huang, C. H. Bartholomew, B. F. Woodfield, *Microporous Mesoporous Mater.* **2014**, *184*, 112–121.
[67] N. M. C. Guari, A. S. Silva, J. L. Diaz de Tuesta, W. E. Pottker, P. Y. Cordeiro, H. T. Gomes, *Global NEST J.* **2022**, *27*, 1–10.

Manuscript received: March 10, 2025
Revised manuscript received: May 26, 2025
Accepted manuscript online: May 29, 2025
Version of record online: June 23, 2025